AGU PUBLICATIONS

Geophysical Research Letters

RESEARCH LETTER
10.1002/2016GL071279

Key Points:
- Near-surface temperature increases with atmospheric mass, and the meridional temperature gradient decreases
- Higher atmospheric heat capacity leads to decreased net radiative cooling
- Suppressed vertical eddy fluxes further warm the lower atmosphere

Supporting Information:
- Supporting Information S1
- Figure S1
- Figure S2
- Figure S3

Correspondence to:
R. Chemke,
rei.chemke@weizmann.ac.il

Citation:
Chemke, R., Y. Kaspi, and I. Halevy (2016), The thermodynamic effect of atmospheric mass on early Earth's temperature, *Geophys. Res. Lett.*, *43*, 11,414–11,422, doi:10.1002/2016GL071279.

Received 19 JUL 2016
Accepted 14 OCT 2016
Accepted article online 18 OCT 2016
Published online 7 NOV 2016

The thermodynamic effect of atmospheric mass on early Earth's temperature

R. Chemke[1], Y. Kaspi[1], and I. Halevy[1]

[1]Department of Earth and Planetary Sciences, Weizmann Institute of Science, Rehovot, Israel

Abstract Observations suggest that Earth's early atmospheric mass differed from the present day. The effects of a different atmospheric mass on radiative forcing have been investigated in climate models of variable sophistication, but a mechanistic understanding of the thermodynamic component of the effect of atmospheric mass on early climate is missing. Using a 3-D idealized global circulation model (GCM), we systematically examine the thermodynamic effect of atmospheric mass on near-surface temperature. We find that higher atmospheric mass tends to increase the near-surface temperature mostly due to an increase in the heat capacity of the atmosphere, which decreases the net radiative cooling effect in the lower layers of the atmosphere. Additionally, the vertical advection of heat by eddies decreases with increasing atmospheric mass, resulting in further near-surface warming. As both net radiative cooling and vertical eddy heat fluxes are extratropical phenomena, higher atmospheric mass tends to flatten the meridional temperature gradient.

1. Introduction

Atmospheric mass plays a key role in planetary habitability. Dense atmospheres may provide protection from high-frequency radiation and can allow the presence of liquid water at the planet's surface by the greenhouse effect, effective heat transport, and various other radiative and convective processes [e.g., *Goldblatt et al.*, 2009; *Wordsworth et al.*, 2011; *Wordsworth and Pierrehumbert*, 2013; *Seager*, 2013; *Charnay et al.*, 2013; *Wolf and Toon*, 2014]. For a better understanding of Earth's early climate, and in particular evidence that Earth was not permanently glaciated in the deep past [*Nutman et al.*, 1997; *Mojzsis et al.*, 2001], despite a fainter Sun [*Gough*, 1981], it is crucial to better understand the relation between atmospheric mass and near-surface temperature.

Various indirect observations suggest that Earth's early atmospheric mass may have differed from its present-day value [e.g., *Nishizawa et al.*, 2007; *Goldblatt et al.*, 2009; *Som et al.*, 2012; *Marty et al.*, 2013; *Johnson and Goldblatt*, 2015; *Kavanagh and Goldblatt*, 2015; *Som et al.*, 2016], though whether the atmosphere was more or less massive than present remains a topic of debate. Negligible atmospheric O_2 concentrations in Earth's early atmosphere [e.g., *Kasting*, 1993] suggest total pressure lower by about 20%, which is unlikely to be compensated for by higher CO_2 concentrations required to explain a relatively warm climate under a weaker early Sun [*Sagan and Chyba*, 2010; *von Paris et al.*, 2008; *Kienert et al.*, 2012; *Wolf and Toon*, 2013; *Wordsworth and Pierrehumbert*, 2013]. The early abundance of the main component of the atmosphere, N_2, is less clear. Earth's geologic N_2 budget suggests that the mantle has been a net sink of N_2, implying greater-than-present Archean atmospheric pressure [*Goldblatt et al.*, 2009; *Johnson and Goldblatt*, 2015], in agreement with upper limits from rain droplet imprints of $2-10$ times the current atmospheric density ~2.7 billion year ago (Ga) [*Som et al.*, 2012; *Kavanagh and Goldblatt*, 2015]. Studies of fluid inclusions in hydrothermal quartz disagree on whether early Archaean atmospheric mass was half today's value or up to 3.3 times greater [*Nishizawa et al.*, 2007; *Marty et al.*, 2013]. Recently, using gas bubbles in basaltic lava, *Som et al.* [2016] suggested an upper limit on surface pressure of only half the present-day value. In aggregate, it appears from existing constraints that the total pressure of the early atmosphere may have been as little as half or as much as 10 times its present-day value.

The range of suggested mass of Earth's early atmosphere has motivated investigations of the climatic effects of a different-than-present mass. These investigations, which employed models of variable complexity, show that an increase in atmospheric mass results in competing effects on temperature at or near the planet's surface. On one hand, molecular (Rayleigh) scattering scales with atmospheric mass, cooling the surface as more

radiation is scattered back to space (higher atmospheric albedo) [e.g., *Goldblatt et al.*, 2009; *Wolf and Toon*, 2014]. On the other hand, radiative-convective climate models show that greater N_2 abundances could have a warming effect due to pressure broadening of the greenhouse gases' (e.g., CO_2 and H_2O) absorption lines [*Goldblatt et al.*, 2009] and due to absorption by H_2-N_2 dimers formed transiently during collisions between H_2 and N_2 [*Wordsworth and Pierrehumbert*, 2013]. In addition, higher sea surface pressure increases the moist adiabatic lapse rate, bringing it closer to the dry lapse rate, suppressing convective fluxes, and further warming the surface [*Goldblatt et al.*, 2009].

Three-dimensional global circulation models (GCMs), which more realistically account for the various components of the climate system, reinforce the findings of 1-D models that with increasing mass the positive radiative forcing due to pressure broadening outweighs cooling due to the increase in Rayleigh scattering [*Wolf and Toon*, 2014] and that convection decreases and modifies the atmospheric temperature lapse rate [*Charnay et al.*, 2013]. Both effects lead to surface warming with increasing atmospheric mass, providing some insight into the dependence of climate on atmospheric mass. However, a systematic investigation of the thermodynamical and dynamical effects has not been conducted to date, preventing a complete understanding of the influence of a different-than-present atmospheric mass on Earth's early near-surface temperature and climate. Using an idealized GCM, *Kaspi and Showman* [2015] showed that the increase in temperature with atmospheric mass is partially due to a decrease in large-scale vertical eddy fluxes, which govern extratropical dynamics [*Vallis*, 2006]. As discussed below, a detailed examination of the effects of increasing atmospheric mass shows that the eddy fluxes in these simulations probably responded to the differential warming caused by changes in the heat capacity of the atmosphere.

In this study, we use an idealized moist GCM to elucidate the effects of atmospheric mass on thermodynamical processes and early Earth's near-surface temperature. The advantage of using an idealized GCM to study the behavior of temperature under variations of atmospheric mass is that compared to 1-D radiative-convective models, an idealized GCM provides a more complete description of the dynamic and thermodynamic structures of the atmosphere (e.g., more realistic vertical and meridional processes). Yet in comparison with full GCMs, which contain a large number of variables that affect the dynamics (e.g., clouds and chemical reactions), the relative simplicity of the idealized GCM enables isolation of the basic physics that contribute most to the dynamic-thermodynamic processes in the atmosphere. We neglect the effects of atmospheric mass on the radiative transfer, which have been previously studied, and focus exclusively on thermodynamic effects.

2. Methodology

2.1. Idealized GCM

To explore the role of atmospheric mass on near-surface temperature, a set of experiments is carried out using an idealized moist atmospheric aquaplanet GCM [*Frierson et al.*, 2006]. The model is a 3-D spherical coordinate primitive equation model of an ideal-gas atmosphere, based on the Geophysical Fluid Dynamics Laboratory flexible modeling system. This model is idealized, in that it is zonally symmetric, and lacks processes that are less relevant for studying the thermodynamic effect of different atmospheric mass (e.g., seasonal and diurnal cycles and clouds). Water vapor is advected in the model with a finite-volume scheme. The surface layer is an ocean slab with no dynamics, which only interacts with the lowest atmospheric layer through heat, moisture, and momentum fluxes. The solar flux is latitudinally distributed at the top of the atmosphere and exponentially decays down to the surface where it is further reflected by a constant global albedo of 0.36. Solar attenuation in the atmosphere does not depend on the atmospheric mass and thus does not account for changes in Rayleigh scattering. The longwave radiative transfer is calculated by a two-stream gray radiation scheme [*Goody and Yung*, 1995; *Held*, 1982], with an optical depth that is a function of latitude and σ ($\sigma = p/p_s$, where p and p_s are the pressure and surface pressure, respectively). The longwave optical depth thus has the same functional form for different p_s and includes neither an increase in the abundance of greenhouse gases with increasing atmospheric mass nor pressure broadening effects [*Frierson et al.*, 2006].

2.2. Simulation Setup

Surface pressure is systematically varied from 0.5 to 10 times Earth's present-day value ($p_{s_e} = 1$ bar), in order to examine the effects of atmospheric mass on the thermodynamics. As the majority of observations constrain Earth's early surface pressure to $0.5-4\times p_{s_e}$, we show the results for this range of p_s in the main text and show the results for $0.5-10\times p_{s_e}$ in the supporting information (Figures S1 and S2). The simulations up to $10\times p_{s_e}$ are similar to the simulations of *Kaspi and Showman* [2015] but with a solar luminosity of 80% of its present-day

value to simulate a weaker early Sun. Each simulation has 30 vertical σ layers at T42 horizontal resolution (2.8° × 2.8°). Increasing the resolution does not have a significant effect on the results. Simulation results presented here are zonally averaged and represent the time average of the last 500 days out of a 1500 day simulation. The major role of the atmospheric heat capacity in these simulations can affect the time it takes the model to reach a thermal and kinetic energy statistically steady state, and in all simulations it is verified that such a steady state is in fact reached. Note that due to the model's simplicity, it may not exactly capture the temperature and wind fields in early Earth's atmosphere. Nevertheless, it enables the study of the 3-D behavior of the dynamic and thermodynamic components of the atmosphere.

Changes in temperature due to increasing atmospheric mass are best understood by studying the model's temperature tendency equation, given by

$$\frac{\partial T}{\partial t} = -\nabla \cdot (\mathbf{u}T) + Q_{\text{adiab}} + Q_{\text{conv}} + Q_{\text{cond}} + Q_{\text{rad}} + Q_{\text{surf}}, \tag{1}$$

where T is the 3-D temperature field, t is time, $\mathbf{u} = (u, v, \omega)$ is the 3-D wind vector in the zonal, meridional, and vertical directions, respectively, $Q_{\text{adiab}} = \frac{\kappa T_v \omega}{p}$ is adiabatic heating, $\kappa = R_d/C_p$, where $C_p = 1004$ J kg^{-1} K^{-1} is the specific heat of air and $R_d = 287$ J kg^{-1} K^{-1} is the gas constant of dry air, T_v is the virtual temperature, and Q_{conv} and Q_{cond} are the convective and condensation heating per unit mass, respectively. The radiative forcing term (Q_{rad}) in equation (1) is given by,

$$Q_{\text{rad}} = \frac{1}{C_p}\frac{\mathrm{d}(S-L)}{\mathrm{d}m}, \tag{2}$$

where S and L are the net solar and longwave radiative fluxes, respectively, and $\mathrm{d}m = \mathrm{d}p/g$ is the atmospheric mass per unit area between every two adjacent vertical levels [*Hartmann*, 1994], where g is the gravitational acceleration. The surface heating (Q_{surf}) includes diffusion and heat fluxes from the surface to the lowest atmospheric layer. In a steady state ($\partial/\partial t = 0$), the two types of processes in equation (1) that are most affected by a change in p_s are moist processes (Q_{conv}), as these involve temperature relaxation toward a moist adiabatic lapse rate [*Betts*, 1986; *Betts and Miller*, 1986; *Frierson et al.*, 2006], and the radiative forcing (Q_{rad}, equation (2)), as it is affected by the atmospheric heat capacity ($C_p\mathrm{d}m$), which increases with increasing atmospheric mass. Studying the temperature tendency equation rather than the energy equation provides a straightforward understanding of the temperature variations due to changes in atmospheric mass, especially as the atmospheric mass affects the heat capacity of the atmosphere, and thus the conversion between energy and temperature.

To isolate the effects of the atmospheric heat capacity and moisture on near-surface (lowest atmospheric level) temperature, under p_s variations, three types of idealized GCM simulations are compared: (I) simulations where both atmospheric heat capacity and moisture effects are taken into account [*Frierson et al.*, 2006], with an active hydrological cycle (i.e., moist convection affects the temperature tendency), and using the radiative forcing term in equation (2). (II) Simulations without moist convection, and using the radiative forcing term in equation (2), and (III) simulations without moist convection and with a forcing scheme based on a Newtonian cooling ($\frac{T_{\text{relax}}-T}{\lambda}$, instead of equation (2)) which does not depend on atmospheric mass [*Held and Suarez*, 1994; *Frierson*, 2005] and where the temperature is relaxed toward a fixed profile (T_{relax}) with a relaxation time λ ($\lambda_i = 150$ days and $\lambda_s = 15$ days are the interior and near-surface relaxation times, respectively), as described in *Schneider* [2004]. In these dry simulations, convection acts to relax the temperature toward a constant convective profile of ~6.8 K km^{-1}. Note that varying λ in type III simulations is equivalent to varying the atmospheric mass in types I and II simulations and thus produces similar results (Figure S3 in the supporting information).

After evaluating the effects of an atmospheric mass different than today's on Earth's early climate using types I–III simulations (section 3.1), we then show and discuss an amplification of the climatic effect of changing atmospheric mass by the positive water vapor and ice-albedo feedbacks (type IA simulations, section 3.2). Since in type I simulations the optical thickness only varies spatially and the planetary albedo is constant, we investigate the effect of these feedbacks, by allowing the water vapor and surface temperature to affect the optical thickness and planetary albedo, respectively (type IA). The setup of type IA simulations is described in section 3.2. Finally, we map the ice line latitude in a parameter space of total and CO_2 surface pressures (section 3.3).

3. Results and Discussion

3.1. Warming Due To an Increase in Atmospheric Mass

The reduction in solar flux to 80% of its present-day value decreases the global mean near-surface temperature to 275 K and pushes the ice line latitude equatorward (the latitude where the near-surface temperature equals the temperature at the triple point of water, $T_0 = 273.16$ K, Figure 1a). Figure 2a shows the change of the mean near-surface temperature in type I simulations with respect to present-day reference simulation (p_{s_e}). When both moisture and atmospheric heat capacity effects are included (type I simulation), the increase in p_s increases the global mean near-surface temperature (Figure 1b) by up to ~4.5 K (at $4 \times p_{s_e}$, red circles in Figure 2a). The convective fluxes may decrease with increasing p_s, due to an increase of the moist adiabatic lapse rate, and thereby increase the near-surface temperature [*Goldblatt et al.*, 2009]. To examine this effect of moisture on the mean near-surface temperature, we performed type II simulations. In these simulations there are no convection processes, and the atmospheric mass only affect the radiative forcing term (equation (2)) through the atmospheric heat capacity ($C_p dm$). In these simulations the temperature increases with surface pressure to ~70–75% of the temperature increase in the moist, type I simulations (blue circles in Figure 2a), demonstrating that moist convection is not the primary cause for the increase of mean near-surface temperature with atmospheric mass. With a radiation scheme independent of pressure (type III simulation), the mean near-surface temperature does not change with p_s (black circles in Figure 2a). Hence, the effects on the mean near-surface temperature due to changes in atmospheric mass are mostly through a change in the atmospheric heat capacity (equation (2)).

The dimmer Sun in Earth's early history leads to stronger global net radiative cooling in the lower atmosphere (i.e., $Q_{\text{rad}} < 0$). The inverse relation between Q_{rad} and the atmospheric mass (equation (2)) decreases net radiative cooling with increasing p_s, thereby increasing the mean near-surface temperature (Figures 1a and 1b and 2a). The presence of the temperature in the radiative forcing term (in the net longwave radiative flux) opposes this warming effect, as the warming itself acts to increase the net radiative cooling, but the overall effect is still a surface warming. Examination of the meridional and vertical temperature distributions reveals a decreased meridional temperature gradient with larger atmospheric mass (compare Figures 1a and 1b). While the near-surface temperature in the tropics warms by ~4 K when the atmospheric mass is quadrupled, at the poles it warms by ~10 K. The meridional distribution of solar heating imposes a net radiative warming at low latitudes, but a net cooling at high latitudes, and overall cooling in the global net, as discussed above. Thus, higher atmospheric mass, which depresses low-latitude radiative warming and high-latitude cooling, tends to flatten the meridional temperature gradient. This may limit baroclinic instability processes [e.g., *Eady*, 1949; *Phillips*, 1954] and, as shown below, may suppress midlatitude vertical eddy temperature fluxes [*Kaspi and Showman*, 2015], thereby trapping heat at the surface and flattening the meridional temperature gradient even further (Figures 1a and 1b), which acts to destabilize the atmosphere [*Stone*, 1978; *Held*, 1982; *Juckes*, 2000; *Schneider*, 2004; *Frierson*, 2006]. Flattening of the gradient is not due to net meridional advection, but due to radiative processes and decreased vertical eddy fluxes.

To better understand the effects of the different components in equation (1) on the mean near-surface temperature at steady state, we calculate their mean values for each value of p_s and compare the results to the present-day reference simulation (p_{s_e}). These results are shown in Figure 2b, where the magnitude of several components in the temperature tendency equation are shown to increase with increasing atmospheric mass. Thus, these components act to warm the near-surface with increasing mass. The increase in magnitude of the warming components is balanced, at a steady state, by a decrease in surface fluxes (orange), leading to less near-surface warming, but this balance is achieved at higher near-surface temperatures with increasing p_s. The radiative component (purple), which contains the effect of the atmospheric heat capacity ($C_p dm$, equation (2)), is the main contributor to near-surface warming. It becomes less negative with increasing p_s, as it decreasingly cools the lower layers of the atmosphere. An associated decrease in vertical eddy advection (blue) traps more heat in the lower atmosphere (compare black contours in Figures 1a and 1b), and contributes to warming with increasing p_s [*Kaspi and Showman*, 2015]. The convection (maroon), mean vertical temperature advection (red), and the adiabatic term (gray) contribute similarly to warming the surface with atmospheric mass, but with a smaller magnitude than the radiation and vertical eddy temperature fluxes. The findings for convection (increased warming with increasing p_s) are similar to the suggested tendency of convective fluxes, at a given surface temperature, to decrease with p_s due to an increase of the moist adiabatic lapse rate [*Goldblatt et al.*, 2009]. However, in relatively massive atmospheres (beyond $3.5 \times p_{s_e}$), the convective fluxes

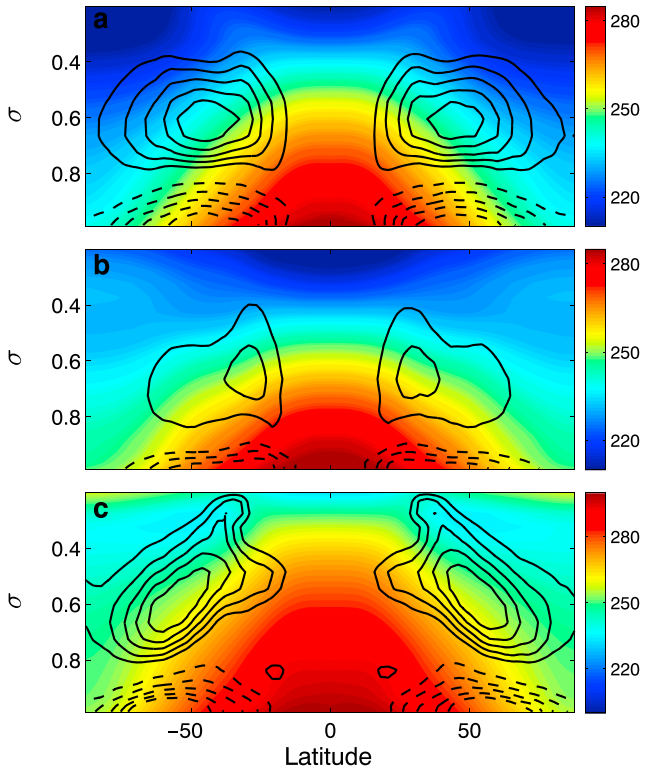

Figure 1. The zonal and time mean temperature (K, color contours) and vertical advection of temperature by eddies (K s^{-1}, black contours) as a function of height and latitude. Solid and dashed contours denote positive and negative temperature tendencies, respectively. (a) Type I simulation of early Earth climate, with solar luminosity of 1088 W m^{-2} (80% its present value) and surface pressure of 1 bar. (b) Type I simulation of early Earth climate, with solar luminosity of 1088 W m^{-2} and surface pressure of 4 bar. (c) Simulation of present-day climate, which includes the greenhouse gas effect of water vapor and ice-albedo feedback, with solar luminosity of 1360 W m^{-2}, surface pressure of 1 bar and 40 Pa of CO_2 at the surface. Minimum and maximum contours correspond to -2.5×10^{-5} and 1×10^{-5} K s^{-1} in Figures 1a and 1c and to -1×10^{-5} and 0.5×10^{-5} K s^{-1} in Figure 1b.

become increasingly negligible, which results in a weaker warming with increasing p_s (Figure S1b in the supporting information). The fact that on one hand, the warming solely due to convection plays a minor role in the temperature tendency equation (maroon circles in Figure 2b), but on the other hand, convection is responsible for almost a third of the warming effect (Figure 2a), suggesting that it triggers other processes that contribute to the warming. These warming effects in the lower atmosphere suppress the sensible and diffusive heat fluxes from the ocean (orange). Changes in the other terms in equation (1) with increasing p_s are of lesser importance (Figure 2b).

3.2. Amplification by Positive Feedbacks

Previous full GCM studies found an increase of ~7 K in the global sea surface temperature for a doubling of surface pressure [*Charnay et al.*, 2013; *Wolf and Toon*, 2014]. Here a doubling of surface pressure produces an increase of only ~2 K. This difference is likely related to two factors. First, the idealized GCM lacks radiative responses to changes in atmospheric mass, such as changes in Rayleigh scattering and, importantly, pressure broadening of infrared absorption by greenhouse gases (e.g., CO_2 and H_2O). Second, positive feedbacks were absent from the simulations in section 3.1, which was aimed at elucidating the thermodynamic effects of different atmospheric mass only. Of these feedbacks, the water vapor and ice-albedo feedbacks are both expected to amplify the temperature response to changes in atmospheric mass. According to the Clausius-Clapeyron relation, the warmer atmospheric column (due to a higher atmospheric mass) holds more water vapor, which increases the infrared opacity of the atmosphere, and may result in additional warming [*Hartmann*, 1994]. Additionally, a warmer surface results in decreased ice cover, and the albedo of the ice itself decreases with increasing temperature [*Griffies et al.*, 2011]. Both effects decrease the planetary albedo, increase the fraction of solar radiation absorbed at the surface, and result in additional warming.

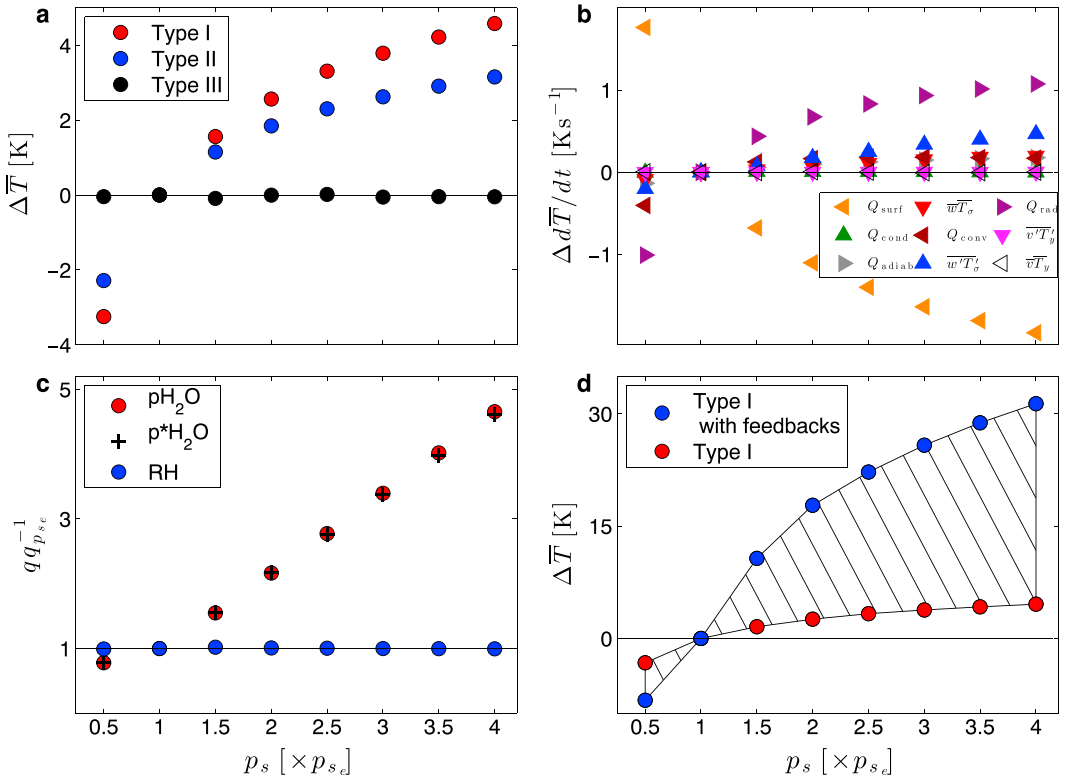

Figure 2. The dependence of zonal, meridional, and time mean near-surface temperature, components of its tendency equation (equation (1)), and moisture parameters on surface pressure relative to the $1 \times p_{s_e}$ simulation with solar luminosity 80% its present value. (a) Mean near-surface temperature from simulations with the effect of heat capacity, and with (type I, red) and without (type II, blue) moist convection, and dry simulations without both moist convection and the effect of heat capacity (type III, black). (b) Mean components of the mean near-surface temperature tendency equation (10^{-5}) in type I simulation at a statistically steady state (i.e., all components add to approximately zero); radiation (purple), vertical advection of eddy temperature fluxes (blue), adiabatic term (gray), vertical advection of mean temperature fluxes (red), meridional advection of mean temperature fluxes (black), meridional advection of eddy temperature fluxes (magenta), surface fluxes (orange), condensation (green), and convection (maroon). (c) The ratio of the tropospheric mean water vapor partial pressure (red), saturated water vapor partial pressure (black crosses), and relative humidity (blue). Shown are simulations with optical thickness calculated using water vapor concentrations and 500 Pa of CO_2 at the surface (type IA). (d) Mean near-surface temperature from simulations with optical thickness calculated using water vapor concentrations and 500 Pa of CO_2 at the surface (blue, type IA) and using parameterized optical thickness (type I, red). The hatched area shows the effect of the water vapor and ice-albedo feedbacks on the mean near-surface temperature.

To account for the greenhouse effect of water vapor and its response to warming (cooling) by an increase (decrease) in atmospheric mass, we run an additional set of simulations (type IA), where the optical depth is not only spatially parameterized as in type I simulations (section 3.1) but also as a function of the water vapor content [*Thuburn and Craig*, 2000; *Merlis and Schneider*, 2010] and CO_2 concentrations. The optical depth varies with height as described in *Frierson et al.* [2006], $\tau = \tau_{CO_2}\sigma + \tau_{H_2O}\sigma^4$, where the linear term represents the relative global contribution of a well-mixed longwave absorber, such as CO_2 and the quadric term represents the relative global contribution of an absorber with a scale height that is one quarter of the pressure scale, such as water vapor. The surface optical depths of CO_2 and water vapor are calculated as the full vertical integral of the absorption coefficient, C, and the number density of the absorber [*Hartmann*, 1994], η, $\tau_{CO_2} = C_1 \int_{p_{top}}^{p_s} \frac{R_d T}{pg} \eta_{CO_2} dp$ and $\tau_{H_2O} = C_2 \int_{p_{top}}^{p_s} \frac{R_d T}{pg} \eta_{H_2O} dp$, respectively. η_{CO_2} and η_{H_2O} are the CO_2 and water vapor number density, respectively. The absorption coefficients, $C_1 = 0.5 \times 10^{-3}$ m^2 and $C_2 = 5 \times 10^{-3}$ m^2, are empirical constants chosen to best produce Earth's current climate (mean near-surface temperature of 289 K, mean meridional temperature gradient between 50 and 60 K, and ice line latitude of ~60°, Figure 1c), with global contributions of water vapor and CO_2 to the net longwave absorption for clear-sky conditions of ~70% and ~30%, respectively [*Kiehl and Trenberth*, 1997; *Schmidt et al.*, 2010], and an increase of 3–4 K for a CO_2 doubling, consistent with the Intergovernmental Panel on Climate Change Fifth Assessment Report

[*Intergovernmental Panel on Climate Change*, 2013]. This, together with the fact that in all simulations the relative humidity changes only by less than ~2% [*Hartmann*, 1994; *Held and Soden*, 2006] (Figure 2c), provides confidence that the qualitative results presented here do not depend on the above adaptation of the radiation scheme.

To account for the ice-albedo feedback, in these simulations (type IA) the albedo is no longer constant but changes with surface temperature [*Griffies et al.*, 2011; *Pierrehumbert et al.*, 2010], T_s, as

$$\alpha\left(T_s\right) = \begin{cases} \alpha_l & T_s \geq T_0 \\ \alpha_h + \left(\alpha_l - \alpha_h\right)\frac{\left(T_s - T_i\right)}{T_0 - T_i} & T_i < T_s < T_0 \\ \alpha_h & T_s \leq T_i \end{cases} \tag{3}$$

where $\alpha_l = 0.26$ and $\alpha_h = 0.45$ are the surface ice-free and ice cover albedo values, respectively, above T_0 the surface is assumed to be ice-free, and $T_i = 263.16$ K is the temperature below which the surface is ice covered.

Although this parameterized radiation scheme is more realistic compared to type I simulations, as it includes water vapor and ice-albedo feedbacks, it still lacks key radiative responses to changes in atmospheric mass (e.g., Rayleigh scattering and pressure broadening of gaseous absorption lines), as well as any responses related to clouds. Changes in cloud cover and, consequently, the planetary albedo may offset some of the warming due to the water vapor and ice-albedo feedbacks. Thus, the radiation scheme used in this study likely tends to underestimate the CO_2 concentrations required to sustain a given mean climate. Conversely, use of this radiation scheme tends to overestimate near-surface temperatures for a given concentration of CO_2. Nevertheless, the idealized GCM with the improved radiation scheme allows an exploration of the thermodynamic response of the atmosphere to changes in mass, and we expect the actual temperature response to be intermediate between the response with and without the water vapor and ice-albedo feedbacks, as parameterized here.

For a constant CO_2 concentration of 500 Pa, including the water vapor and ice-albedo feedbacks results in substantial warming as the mass of Earth's atmosphere increases (Figure 2d, blue). For example, with $p_s = 2 \times p_{s_e}$ the global average near-surface temperature increases by more than 15 K (compared to ~2 K without the feedbacks). With $p_s = 4 \times p_{s_e}$ the global average near-surface temperature increases by ~30 K (compared to ~4.5 K without the feedbacks). This is double the warming found in full GCMs [*Charnay et al.*, 2013; *Wolf and Toon*, 2014], probably due to the absence of Rayleigh scattering in our simulations, which increases with atmospheric mass [*Wolf and Toon*, 2014]. The warming can be divided into effects arising only from the increased atmospheric mass (Figure 2d, red), which are discussed in section 3.1, and those arising from positive feedbacks due to the atmospheric water vapor content and the albedo of ice, which together account for the majority of the warming (Figure 2d, hatched area). It is important to note, however, that the positive feedbacks are only pushed into operation by the warming associated with an increase in atmospheric mass.

3.3. Ice Line Latitude and Earth's Habitability

A necessary condition for Earth's early habitability is that the ice line latitude is poleward of the tropics and global glaciation is avoided. The ice line latitude shifts poleward with increasing pCO_2 due to a stronger greenhouse effect (Figure 3), consistent with the findings of previous studies [*Pierrehumbert et al.*, 2010]. In addition, even with constant pCO_2, the ice line latitude shifts poleward with increasing p_s. At ~3 Ga (80% present luminosity) and pCO_2 between 300 and 600 Pa (within observational constraints) [*Kasting*, 2010, and references therein], an atmospheric mass 1 to 3 times its present-day value is sufficient to achieve a present-day ice line latitude of ~60°. At ~3.8 Ga (75% present luminosity) an atmospheric mass 2 to 5 times its present value is sufficient for the same range of pCO_2 (Figure 3b). Overall, a more massive early atmosphere may help to explain the existence of liquid water on Earth's surface in the face of a less luminous early Sun.

The rate of increase of the ice line latitude with surface pressure depends on pCO_2 (see the contour gradient upon a horizontal transect in Figure 3). As mentioned above, the decrease in both net radiative cooling and vertical eddy temperature fluxes, which are more pronounced in the extratropics [*Vallis*, 2006], preferentially warms the high latitudes as surface pressure is increased. As a result, when pCO_2 is high and the ice line resides at relatively high latitudes, which are more sensitive to a change in atmospheric mass, the change in ice line latitude due to changing atmospheric mass is more pronounced. This also affects the termination of global glaciations. The global net warming due to increasing p_s leads to a requirement of less CO_2 to initiate deglaciation. In addition, as discussed above, once deglaciation starts, as the ice line latitude resides further

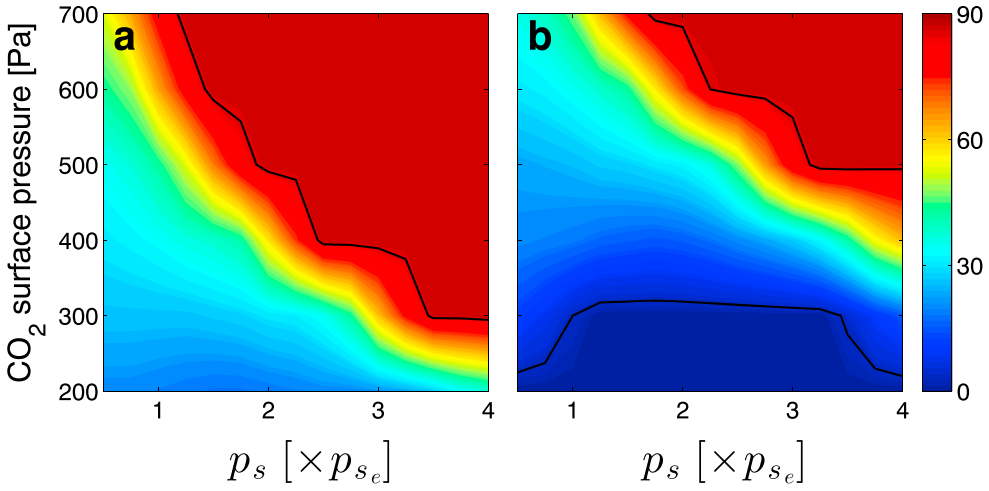

Figure 3. Ice line latitude as a function of pCO_2 and total surface pressure. Shown are simulations with the water vapor and ice-albedo feedbacks and with a solar luminosity of (a) 80% and (b) 75% its present value. The black contours represent the 90° and 0° ice line latitudes. The total surface pressure and pCO_2 simulations are conducted in intervals of $0.25 \times p_{s_e}$ and 100 Pa, respectively.

poleward, for a given pCO_2, it increases more rapidly with increasing p_s. This effect can be seen in Figure 3b, where a shift in the ice line from snowball (lower black line) to ice-free (upper black line) conditions requires smaller ΔpCO_2 with increasing p_s. Note that at low p_s and CO_2 concentrations, the ice line latitude decreases with atmospheric mass (bottom-left corner in Figure 3b). This may be related to near-surface condensation, due to the low temperatures. The associated release of latent heat may result in a poleward shift of the ice line with decreasing atmospheric mass.

4. Conclusions

An increase (decrease) in atmospheric mass causes an increase (decrease) in near-surface temperatures and a decrease (increase) of the equator-to-pole near-surface temperature gradient. Warming is caused mostly by the increase in atmospheric heat capacity with mass, which decreases the net radiative cooling of the atmosphere. Also important is a decrease in vertical eddy heat fluxes, which traps more heat in the lower atmosphere and heats the surface. As both net radiative cooling and vertical heat fluxes are more pronounced at middle-high latitudes, the meridional temperature gradient decreases with increasing atmospheric mass. A more massive atmosphere would have required lower greenhouse gas abundances to maintain a warm climate on early Earth, perhaps to within constraints on paleo-pCO_2 levels. On the other hand, if Earth's early atmosphere was less massive, as suggested in some recent studies, then higher abundances of greenhouse gases, or other warming mechanisms, would have been required to keep Earth's surface warm.

Acknowledgments
We thank Daniel Koll and Thaddeus Komacek whose comments have helped to improve the manuscript. The data in the manuscript may be obtained from Rei Chemke (rei.chemke@weizmann.ac.il). R.C. was funded by a Lev-Zion fellowship. Y.K. was funded by the Israeli Ministry of Science. I.H. was funded by a European Research Council Starting grant 337183.

References

Betts, A. K. (1986), A new convective adjustment scheme. Part I: Observational and theoretical basis, *Q. J. R. Meteorol. Soc.*, *112*, 677–691.
Betts, A. K., and M. J. Miller (1986), A new convective adjustment scheme. Part II: Single column tests using GATE wave, BOMEX, ATEX and arctic air-mass data sets., *Q. J. R. Meteorol. Soc.*, *112*, 693–709.
Charnay, B., F. Forget, R. Wordsworth, J. Leconte, E. Millour, F. Cordon, and A. Spiga (2013), Exploring the faint young sun problem and the possible climates of the Archean Earth with a 3-D GCM, *J. Geophys. Res. Atmos.*, *118*, 10,414–10,431, doi:10.1002/jgrd.50808.
Eady, E. T. (1949), Long waves and cyclone waves, *Tellus*, *1*(3), 33–52.
Frierson, D. M. W. (2005), Studies of the general circulation with a simplified moist general circulation model, PhD thesis, 218 pp., Princeton Univ., N. J.
Frierson, D. M. W. (2006), Robust increases in midlatitude static stability in simulations of global warming, *Geophys. Res. Lett.*, *33*, L24816, doi:10.1029/2006GL027504.
Frierson, D. M. W., I. M. Held, and P. Zurita-Gotor (2006), A gray-radiation aquaplanet moist GCM. Part I: Static stability and eddy scale, *J. Atmos. Sci.*, *63*(10), 2548–2566.
Goldblatt, C., M. W. Claire, T. M. Lenton, A. J. Matthews, A. J. Watson, and K. J. Zahnle (2009), Nitrogen-enhanced greenhouse warming on early Earth, *Nat. Geosci.*, *2*(12), 891–896.
Goody, R. M., and Y. L. Yung (1995), *Atmospheric Radiation: Theoretical Basis*, 519 pp., Oxford Univ. Press, New York
Gough, O. D. (1981), Solar interior structure and luminosity variations, in *Physics of Solar Variations*, pp. 21–34, Springer, Netherlands.
Griffies, S. M., et al. (2011), The GFDL CM3 coupled climate model: Characteristics of the ocean and sea ice simulations, *J. Clim.*, *24*, 3520–3544.

Hartmann, D. L. (1994), *Global Physical Climatology*, Academic Press, San Diego, Calif.
Held, I. M. (1982), On the height of the tropopause and the static stability of the troposphere, *J. Atmos. Sci.*, *39*(2), 412–417.
Held, I. M., and B. J. Soden (2006), Robust responses of the hydrological cycle to global warming, *J. Clim.*, *19*, 5686–5699.
Held, I. M., and M. J. Suarez (1994), A proposal for the intercomparison of the dynamical cores of atmospheric general circulation models, *Bull. Am. Meteorol. Soc.*, *75*, 1825–1830.
Intergovernmental Panel on Climate Change (2013), Summary of policymakers, in *Climate Change 2013: The Physical Basis*, edited by T. F. Stocker et al., pp. 1–29, Cambridge Univ. Press, New York.
Johnson, B., and C. Goldblatt (2015), The nitrogen budget of Earth, *Earth Sci. Rev.*, *148*, 150–173.
Juckes, M. N. (2000), The static stability of the midlatitude troposphere: The relevance of moisture, *J. Atmos. Sci.*, *57*, 3050–3057.
Kaspi, Y., and A. P. Showman (2015), Three dimensional atmospheric dynamics of terrestrial exoplanets over a wide range of orbital and atmospheric parameters, *Astrophys. J.*, *804*, 60.
Kasting, J. F. (1993), Earth early atmosphere, *Science*, *259*(5097), 920–926.
Kasting, J. F. (2010), Early Earth: Faint young sun redux, *Nature*, *464*(7289), 687–689.
Kavanagh, L., and C. Goldblatt (2015), Using raindrops to constrain past atmospheric density, *Earth Planet. Sci. Lett.*, *413*, 51–58.
Kiehl, J. T., and K. E. Trenberth (1997), Earth's annual global mean energy budget, *Bull. Am. Meteorol. Soc.*, *78*(2), 197–208.
Kienert, H., G. Feulner, and V. Petoukhov (2012), Faint young sun problem more severe due to ice-albedo feedback and higher rotation rate of the early Earth, *Geophys. Res. Lett.*, *39*, L23710, doi:10.1029/2012GL054381.
Marty, B., L. Zimmermann, M. Pujol, R. Burgess, and P. Philippot (2013), Nitrogen isotopic composition and density of the Archean atmosphere, *Science*, *342*, 101–104.
Merlis, T. M., and T. Schneider (2010), Atmospheric dynamics of Earth-like tidally locked aquaplanets, *J. Adv. Mod. Earth Syst.*, *2*(4), 13, doi:10.3894/JAMES.2010.2.13.
Mojzsis, S. J., T. M. Harrison, and R. T. Pidgeon (2001), Oxygen-isotope evidence from ancient zircons for liquid water at the Earth's surface 4,300 Myr ago, *Nature*, *409*(6817), 178–181.
Nishizawa, M., Y. Sano, Y. Ueno, and S. Maruyama (2007), Speciation and isotope ratios of nitrogen in fluid inclusions from seafloor hydrothermal deposits at ~3.5 GA, *Earth Planet. Sci. Lett.*, *254*, 332–344.
Nutman, A. P., S. J. Mojzsis, and C. R. Friend (1997), Recognition of ≥3850 Ma water-lain sediments in West Greenland and their significance for the early Archaean Earth, *Geochim. Cosmochim. Acta*, *61*, 2475–2484.
Phillips, N. A. (1954), Energy transformations and meridional circulations associated with simple baroclinic waves in a two level quasi-geostrophic model, *Telus*, *6*(3), 273–286.
Pierrehumbert, R. T., D. S. Abbot, A. Voigt, and D. Koll (2010), Climate of the neoproterozoic, *Annu. Rev. Earth Planet. Sci.*, *39*(1), 417–460.
Sagan, C., and C. Chyba (2010), The early faint sun paradox: Organic shielding of ultraviolet-labile greenhouse gases, *Science*, *276*(5316), 1217–1221.
Schmidt, G. A., R. A. Ruedy, R. L. Miller, and A. A. Lacis (2010), The attribution of the present-day total greenhouse effect, *J. Geophys. Res.*, *155*, D20106, doi:10.1029/2010JD014287.
Schneider, T. (2004), The tropopause and the thermal stratification in the extratropics of a dry atmosphere, *J. Atmos. Sci.*, *61*(12), 1317–1340.
Seager, S. (2013), Exoplanet habitability, *Science*, *340*, 577–581.
Som, S. M., D. C. Catling, J. P. Harnmeijer, P. M. Povlika, and R. Buick (2012), Air density 2.7 billion years ago limited to less than twice modern levels by fossil raindrop imprints, *Nature*, *484*(7394), 359–362.
Som, S. M., R. Buick, J. W. Hagadorn, T. S. Blake, J. M. Perreault, J. P. Harnmeijer, and D. C. Catling (2016), Earth's air pressure 2.7 billion years ago constrained to less than half of modern levels, *Nat. Geosci.*, *9*, 448–451.
Stone, P. H. (1978), Baroclinic adjustment, *J. Atmos. Sci.*, *35*(4), 561–571.
Thuburn, J., and G. C. Craig (2000), Stratospheric influence on tropopause height: The radiative constraint, *J. Atmos. Sci.*, *57*, 17–28.
Vallis, G. K. (2006), *Atmospheric and Oceanic Fluid Dynamics*, 770 pp., Cambridge Univ. Press, Cambridge, U. K.
von Paris, P., H. Rauer, J. Lee Grenfell, B. Patzer, P. Hedelt, B. Stracke, and F. Schreier (2008), Warming of the early Earth—CO_2 reconsidered, *Planat. Space Sci.*, *56*(9), 1244–1259.
Wolf, E. T., and O. B. Toon (2013), Hospitable Archean climates simulated by a general circulation model, *Astrobiology*, *13*(7), 656–673.
Wolf, E. T., and O. B. Toon (2014), Controls on the Archean climate system investigated with a global climate model, *Astrobiology*, *14*, 241–253.
Wordsworth, R., and R. Pierrehumbert (2013), Hydrogen-nitrogen greenhouse warming in Earth's early atmosphere, *Science*, *339*(6115), 64–67.
Wordsworth, R. D., F. Forget, F. Selsis, E. Millour, B. Charnay, and J.-B. Madeleine (2011), Gliese 581d is the first discovered terrestrial-mass exoplanet in the habitable zone, *Astrophys. J. Let.*, *733*, L48.